CHEMISTRY OF MATERIALS

Article

pubs.acs.org/cm

Lithium Lanthanum Titanium Oxides: A Fast Ionic Conductive Coating for Lithium-Ion Battery Cathodes

Danna Qian, Bo Xu, Hyung-Man Cho, Toru Hatsukade, Kyler J. Carroll, and Ying Shirley Meng*

Department of NanoEngineering, University of California−San Diego, 9500 Gilman Drive, La Jolla, California 92093, United States

Supporting Information

ABSTRACT: This work introduces Li−La−Ti−O (LLTO), which is a fast lithium-ion conductor, as an effective coating material for cathode materials used in rechargeable lithium-ion batteries. This fast Li-ion conductor is characterized by first-principles calculations showing low activation barrier for lithium diffusion at various different lithium concentrations. The morphology and the microstructure of the pristine electrode and coated electrode materials are characterized systematically, and we show clear evidence of the presence of the coating after electrochemical cycling. The coated electrodes show significantly improved rate capabilities and cycling performance, compared to the pristine electrodes. The possible reasons for such enhancements are explored experimentally using potentiostatic intermittent titration technique (PITT), electrochemical impedance spectroscopy (EIS). Because of the high lithium conductivity in the LLTO coating material, the chemical Li^+ diffusion coefficient is one magnitude of order higher in the coated samples than that in the uncoated samples. In addition, the impedances of both interfacial charge transfer and Li^+ transportation in the solid-electrolyte-interphase (SEI) layer are reduced up to 50% in the coated samples. Our findings provide significant insights into the role of coating regarding the improvements of electrochemical properties, as well as the potential use of solid electrolyte as an effective coating material.

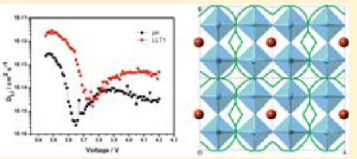

KEYWORDS: *lithium ion batteries, lithium lanthanum titanate, fast lithium ion conductor, first principles calculations, GGA+U, solid electrolyte*

1. INTRODUCTION

Lithium lanthanum titanate (LLTO) is one of the fastest lithium-ion conductors to date. $Li_{3x}La_{(2/3)-x}\square_{(1/3)-2x}TiO_3$ adopts the perovskite structure ABO_3 with A = Li, La, and B = Ti.[1−6] This series of materials are considered to have fast lithium transportation and the bulk ionic conductivity can be achieved as high as 1×10^{-3} S cm^{-1} at room temperature when $x = 0.11$.[7,8] Applying this material as the solid electrolyte in all-solid Li-ion battery is under intensive studies.[9−11]

At present, the electrolyte of secondary lithium-ion batteries in the market is mainly based on $LiPF_6$ salt dissolved in an organic solvent (such as ethylene carbonate). Electrolyte needs to be a fast Li ion conductor, but an electron insulator. A major concern about the liquid electrolyte is the safety issue, including poor thermal stability and low resistance to leakage. In addition, conventional electrolyte has narrow voltage window, decomposition would happen at both extremely low and high voltage ranges causing electrode/electrolyte parasitic reactions. Upon cycling, the electrolyte would get consumed and the cell eventually fails. Solid electrolyte can mitigate these problems but to have fabricate a continuous layer of solid electrolyte layer at large dimensions remains a major challenges. In this study, we are applying solid electrolyte as a coating material for cathode in lithium-ion batteries to resolve the current issues in the second-generation layered transition-metal oxide materials, such as $LiNi_{0.8}Co_{0.15}Al_{0.05}O_2$ (NCA).

The current problems (fading capacity and poor cyclability, etc.) present in pristine NCA layered cathode material have been attributed to the dissolution of the cation into the electrolyte, as well as the surface layer-to-spinel phase transformation happening in most layered materials.[12] Coatings such as AlF_3, ZrO_2, Al_2O_3, etc. have been studied intensively to improve the performance. Suppression of the phase transitions, increases in the structural stabilities, as well as decreases in the disorder of cations in the crystal sites have been observed. However, the surface modification mechanism still remains open for different coating materials. Furthermore, few studies have been reported on the characterization of continuous effect of coating upon cycling.

In this study, first-principles calculations were performed to explore the lithium diffusion pathways and calculate the lithium diffusion activation barriers in $Li_{3x}La_{(2/3)-x}\square_{(1/3)-2x}TiO_3$, when $3x = 0.125$ and 0.35. To study the effect of LLTO as a coating for cathodes, the LLTO coating has been applied to $LiNi_{0.8}Co_{0.15}Al_{0.05}O_2$ (NCA). We show significantly improved electrochemical performances of the coated samples. To systematically study the mechanism of a solid electrolyte as a coating material to cathode, scanning electron microscopy (SEM), energy-dispersive spectroscopy (EDS), X-ray diffraction (XRD), and transmission electron microscopy (TEM), combined with electrochemical property measurements including PITT and EIS were carried out on both the pristine NCA sample and the LLTO-coated sample. SEM analysis coupled with electron energy loss spectroscopy (STEM_EELS)

Received: March 23, 2012
Revised: June 20, 2012

   dx.doi.org/10.1021/cm300929r | *Chem. Mater.* XXXX, XXX, XXX−XXX

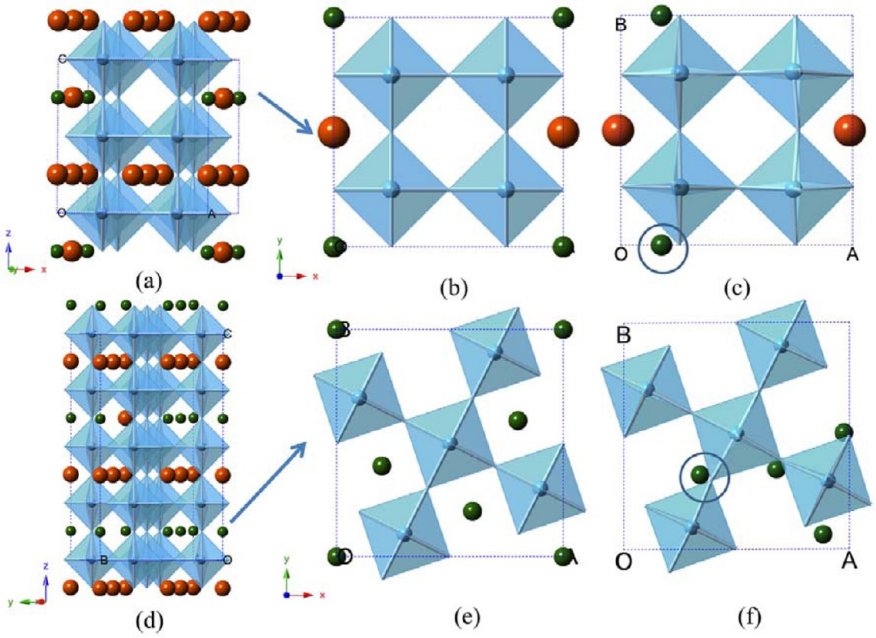

Figure 1. (a) Computational model structure of $Li_{0.125}La_{0.625}TiO_3$. (b) Planes of interest used in NEB calculation of low lithium concentration. (c) After-relaxation structure of planes in panel b. (d) Computational model structure of $Li_{0.35}La_{0.55}TiO_3$. (e) Planes of interest used in NEB calculation of high lithium concentration. (f) After-relaxation structure of planes in panel e. Green sphere is Li, yellowish brown is La, and blue octahedral is Ti surrounded by six O (oxygen ions at the vertices of the polyhedron are omitted for clarity).

mapping was performed on a coated sample and data were collected before and after cycling.

2. EXPERIMENTAL SECTION

Computational Methodology. In this work, two models of $Li_{3x}La_{(2/3)-x}\square_{(1/3)-2x}TiO_3$ are created with low lithium concentration (x = 1/24) and high lithium concentration (x = 7/60). For low-lithium-concentration LLTO, the atomic models and notations are adopted from previous work done by Catti.[15,16] The supercell is composed of eight formula units of $Li_{0.125}La_{0.625}TiO_3$. For high-lithium-concentration LLTO, an original model is proposed in this study with 20 formula units of $Li_{0.35}La_{0.55}TiO_3$. First-principles calculations were performed in the spin-polarized GGA+U approximation to the density functional theory (DFT). Core electron states were represented by the projector augmented-wave method,[17] as implemented in the Vienna ab initio simulation package (VASP).[18,19] The Perdew–Burke–Ernzerhof (PBE) correlation[18] and a plane wave representation for the wave function with a cutoff energy of 420 eV were used. The Brillouin zone was sampled with a mesh including a gamma point. The density of the k-point mesh for all calculations is approximately one point per 0.01 $Å^{-3}$.The atomic positions and cell parameters were fully relaxed to obtain total energy and optimized cell structure. An effective U value is applied in the Liechtenstein approach with exchange energy J = 1.0 eV.[20,21] U_{eff} = 7.5 eV is applied to the La 4f states to correct their position relative to La 5d levels.[22] It is reported that the experimentally observed position of 4f bands can be reproduced within this approach.[23] The Nudged Elastic Band (NEB) method is used to find the minimum energy path and the energy barrier for Li diffusion in LLTO.[24]

Experimental Methodology. *Materials.* All the samples, an NCA pristine sample with a particle size of ~100 nm, together with 1, 2, and 5 wt % LLTO-coated NCA samples (named as LLT1, LLT2, and LLT5, respectively), were synthesized by CheMat Technology.

Materials Characterization. The particle morphology and size distribution of the synthesized powders were determined using an FEI XL30UHR SEM (ultrahigh-resolution SEM) system with a Sirion column, which enables very-high-resolution imaging at low kV. All images were collected under an accelerating voltage of 10 kV. The powders were suspended on a double-sided carbon tape placed on a specimen holder.

EDS was taken using a Phillips XL30 field-emission environmental high-resolution SEM with an Oxford EDS attachment.

XRD spectra were taken using a Bruker D8 advance diffractometer with a Bragg–Brentano θ–2θ geometry and a Cu Kα source. Samples were scanned from 10° to 80° with a scan rate of 0.025° per second.

TEM images were collected using an FEI Tecnai G2 Sphera cryo-electron microscope with an operation voltage of 200 kV. The powders were suspended on a 300-mesh copper grid with lacey carbon.

STEM-EELS data was collected using a Cs-corrected FEI Titan 80/300-kV TEM/STEM microscope equipped with a Gatan Image Filter Quantum-865. All STEM images were acquired at 300 kV. EELS spectra shown in this work were acquired with a convergence angle of 30 mrad.

Electrochemical Characterization. Cathodes were prepared by mixing 80 wt % pristine and coating powder with 10 wt % acetylene carbon black (99.9%) and 10 wt % poly(vinylidene fluoride) in *N*-methyl pyrrolidone solution. The slurry was cast onto Al foil using a doctor blade and dried overnight in a vacuum oven at 80 °C. The electrode disks were punched and dried again at 80 °C for 6 h before storing them in an argon-filled glovebox (H_2O level of <1 ppm). 2016-type coin cells were used to study the electrochemical behavior of the compounds. Lithium metal ribbon and 1 M $LiPF_6$ in a 1:1 EC:DMC solutions were used as the anode and electrolyte, respectively. A Model C480 separator (Celgard, Inc.) was used as the separator. The coin cells were assembled in the same argon-filled glovebox and tested on an Arbin battery cycler in galvanostatic mode. The cycling tests were conducted between 2.5 V and 4.2 V, and the rate tests were in the window of 2.0–4.4 V.

The PITT experiments were carried out by applying potential steps of 10 mV and measuring the current as a function of time for the first charge. The potential step was advanced to the next level when the measured current fell below the threshold limit of 10 μA, corresponding to a C/200 rate. The voltage window was set at 3.45–4.2 V.

Solartron 1287 system coupled with a Solartron 1260 frequency response analyzer was used for the EIS measurement. The EIS test was carried out using the three-electrode cell. For the reference electrode,

dx.doi.org/10.1021/cm300929r | *Chem. Mater.* XXXX, XXX, XXX–XXX

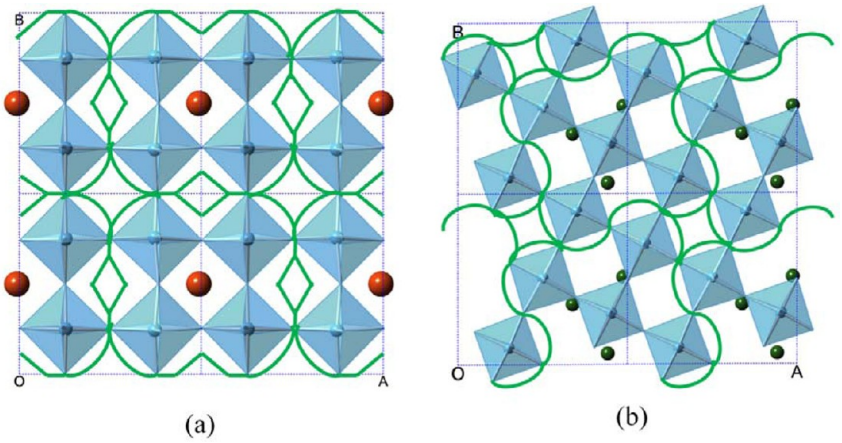

Figure 2. Estimated Li diffusion path in La-poor layer (green dashed lines) in (a) the low-lithium-concentration scenario and (b) the high-lithium-concentration scenario.

the end tip of the Teflon-coated Cu wire (ϕ(Teflon) = 4.5 × 10^{-4} m; ϕ(Cu) = 1.27 × 10^{-4} m) was removed and placed between two separators. Details on cell configuration can be found elsewhere.[13,14] Before the electrochemical experiments, elemental Li was cathodically coated on the bare Cu wire by having Li metal as a counter electrode. The as-prepared cell was charged to and equilibrated at 4.2 V at a rate of C/10. The impedance spectra were obtained in the frequency range of 100 kHz to 100 mHz.

3. RESULTS

3.1. Computational Results. *3.1.1. Low Lithium Concentration Scenario.* The atomic structure of $Li_{0.125}La_{0.625}TiO_3$ is shown in Figure 1a. For low-lithium-concentration LLTO, the atomic models and notations are adopted from previous work done by Catti et al.[15,16] The supercell is composed of $2a_p$ × $2a_p$ × $2a_p$, where a_p is the conventional cubic lattice of ABO_3 perovskite structure (38 atoms in total). La ions are located in A sites and Ti ions in B sites. Li ions are also located in A sites as initialization. Along the (001) direction, four A-site ions in the (001) plane can be grouped as a two-dimensional (2D) cell. A La-rich layer (z = 1/4) is composed of 4 La ions (4La) and a La-poor layer (z = 3/4) composed of 1 La ion, 1 Li ion, and 2 vacancies (1La + 1Li + 2□) (shown in Figure 1b). This La-rich and La-poor layers are alternatively arranged, according to the experimental observations.[25] The after-relaxation structure of the z = 3/4 plane is shown in Figure 1c. After structural relaxation, the cubic lattice is distorted to an orthorhombic lattice, where a = 7.828 Å, b = 7.754 Å, c = 7.871 Å. La and Ti ions are still in A and B sites, respectively, while Li ions move closely to the center vertical oxygen square planar window as shown in Figures S1b and S1c in the Supporting Information. These results are consistent with the previous work.[16] These sites are referred as Li equilibrium sites in this work. Figure S1a in the Supporting Information shows all the Li equilibrium sites in the 2D La-poor layer. These equilibrium sites are used as the end-points of the NEB calculations and the corresponding energies are used as the references when calculating Li diffusion activation barriers. Based on the NEB calculation results, when Li ions diffuse between two equilibrium sites, they prefer a curved diffusion path that avoids the empty A sites (Figure 2a). The crosses in Figure S1a in the Supporting Information are the saddle points in the calculated minimum energy paths for Li diffusion. The obtained energy barriers are 230 meV (from Li1 to Li2) and 22 meV (from Li2 to Li3), which is much lower than the previous values reported by Catti et al.[16] The discrepancy may be from the following possible reasons: first, our predicted pathway is different, which was obtained by NEB method instead of the "Frozen Ion" method adopted by previous work. NEB has been proved to be pretty reliable on predicting the pathways and finding minimum energy path on the potential energy surface (PES). Second, different DFT functionals were used. However, we believe the U correction is not playing a role. Besides the data shown in this work, we have also calculated the pathway and diffusion barriers without U correction, which gives us consistent results.

3.1.2. High-Lithium-Concentration Scenario. The same method used in calculations of the low-lithium-concentration model is adopted for the high-lithium-concentration scenario $Li_{0.35}La_{0.55}TiO_3$. In all cases, space group $P1$ is used to reduce the symmetry constrains to a minimum. It is a supercell composed of $\sqrt{5}a_p$ × $\sqrt{5}a_p$ × $4a_p$. The 2D cell in the (001) plane is composed of five A-sites occupied by Li, La, or vacancies. Three different models are established with different in-plane cation arrangements and the layer stacking sequences. Similar to the low-lithium-concentration model, La-rich and La-poor layers are alternatively arranged; in addition, because of La ion's large radii and its strong interactions with Li ions, the principle of as little La in the Li layer as possible is adopted in this model. The calculated energies are listed in Table S1 in the Supporting Information. Because of the structure complexity, our investigations are focused on the La-poor layer (z = 1/8, 4Li + 1□) of model I, which is the lowest in energy among the proposed models, drawn in Figure 1d. This model can be rationalized that by having the least number of La in the La-poor layer helps reducing the repulsion forces and results in the lowest energy. The corresponding 2D cell of the La-poor layer (z = 1/8) is shown in Figure 1e, and the structure of this layer after relaxation is depicted in Figure 1f. After structural relaxation, Li equilibrium sites are also close to the center of vertical oxygen square window, similar to the results obtained in the low-lithium-concentration scenario. NEB calculations are performed to find the diffusion paths and energy barrier for the circled Li. A similar curved diffusion path can be found as shown in Figure 2b. The minimum energy path avoids both the empty A-site and the three other Li ions. The highest activation barrier for this diffusion path is ∼390 meV, and there also are barriers in other local environments at ∼120 meV within this path.

dx.doi.org/10.1021/cm300929r | *Chem. Mater.* XXXX, XXX, XXX–XXX

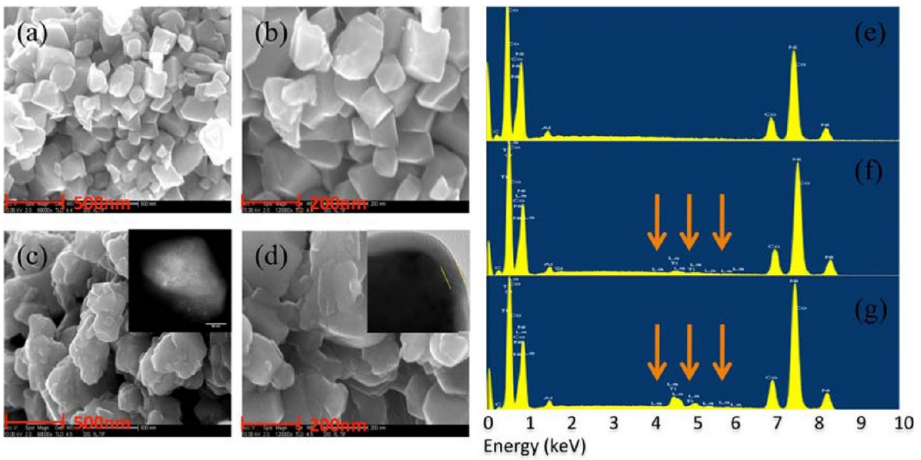

Figure 3. Structural characterization of pristine and LLTO-coated samples: (a, b) SEM images of pristine samples; (c, d) SEM images of LLT5, respectively; (e) EDS results of the pristine sample; (f) EDS results of the LLT1 sample; and (g) EDS results of the LLT5 sample. The yellow arrows are used to indicate the signal of elements La and Ti. The inset in panels c and d is the TEM image of LLT5.

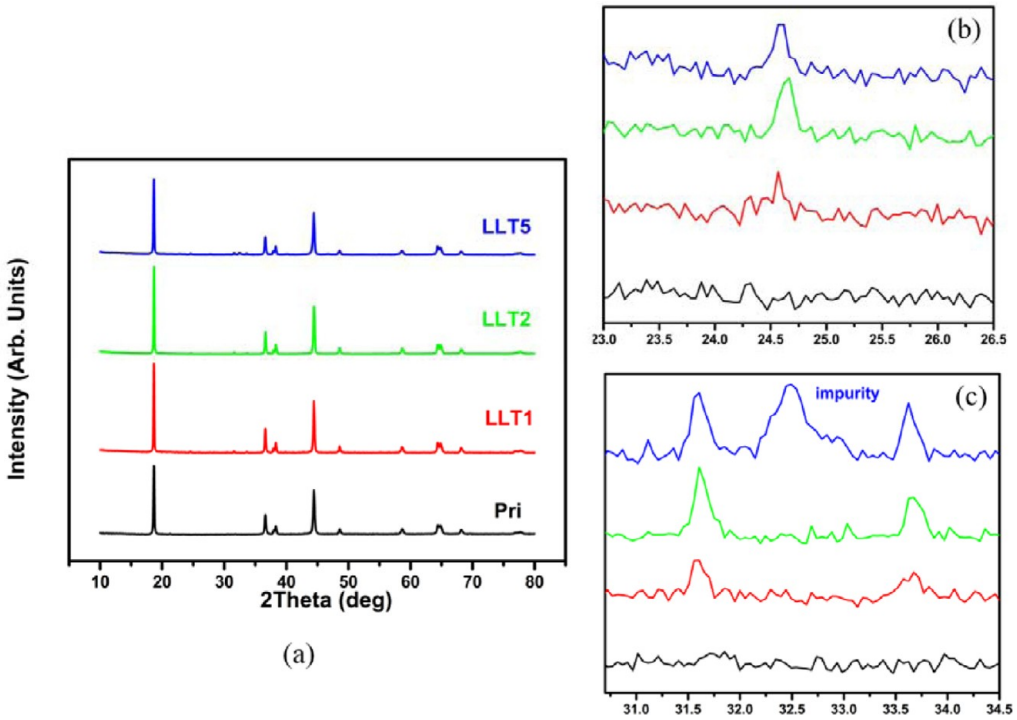

Figure 4. (a) XRD results of pristine (black trace), LLT1 (red trace), LLT2 (green trace), and LLT5 (blue trace). (b) Enlargement of the 23°−26.5° region. (c) Enlargement of the 30.5°−34.5° region.

3.2. Experimental Results. *3.2.1. Materials Characterization: SEM/EDS, XRD, and TEM.* The morphology of pristine and LLTO coated powders were examined by scanning electron microscopy (SEM) (Figures 3a−d). The pristine particles have a very uniform size distribution of ∼100 nm. The primary particle size after the LLTO coating is slightly increased, ranging between nm 100 and 200 nm. It is hypothesized that some sintering of primary particles may have occurred during the LLTO coating process, as can be seen in the SEM images. From Figure 4a, the XRD data of pristine, 1 wt % LLTO-coated (LLT1), 2 wt % LLTO-coated (LLT2), and 5 wt % LLTO-coated (LLT5) samples shows that the main peaks are representative of the layered structure $LiNi_{0.8}Co_{0.15}Al_{0.05}O_2$ with the $R\bar{3}m$ symmetry group; in addition, the existence of doublets at (006)/(102) and (108)/(110) indicates the well-layered structure with little Li/Ni interlayer mixing. In Figures 4b and 4c, the most intense peaks are associated with the LLTO phase[26]—2θ = 24.6°, 31.6°, 33.6°—and appear for all three coated samples. All three peaks, however, shifted to a lower angle, compared to the published data on the bulk of LLTO,[26] which indicates larger interplane distances in the LLTO coating. Figures 3e−g respectively show the EDS results of pristine, LLT1, and LLT5 samples, which indicates that the amount of La and Ti elements increases with the coating weight percentage.

To further investigate the surface morphology of pristine and coated materials, TEM images were taken. The surface coating is mostly similar to small islands distributed on the surface of pristine material (see inset in Figure 3c; the white spots indicate the coating material). In addition, some particles were coated

dx.doi.org/10.1021/cm300929r | Chem. Mater. XXXX, XXX, XXX−XXX

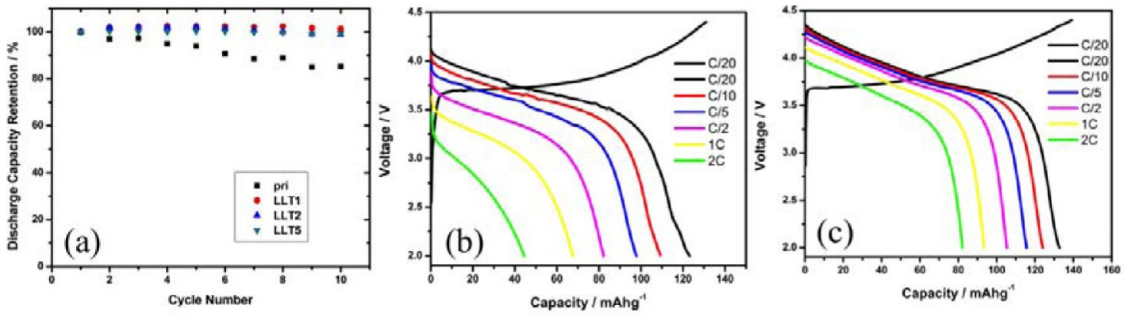

Figure 5. Electrochemical cycling and rate capability of pristine and coated electrodes: (a) cycling retention properties of pristine, LLT1, LLT2, and LLT5. (b) Rate capability of the pristine sample. (c) Rate capability of the LLT1 sample.

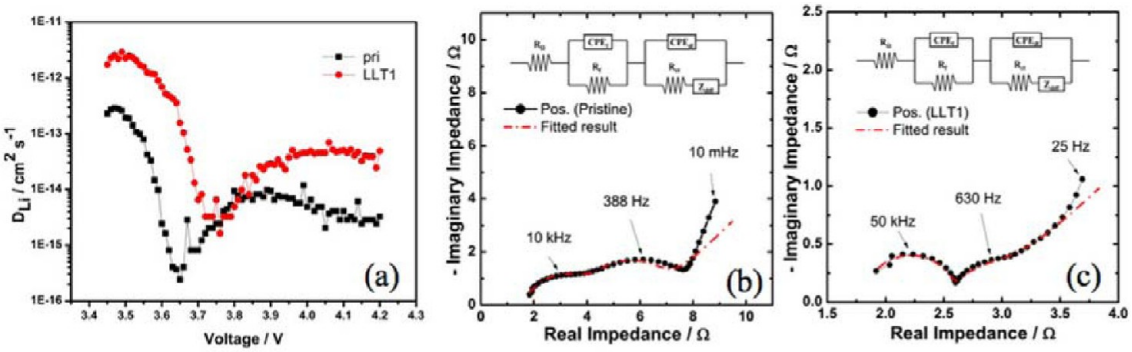

Figure 6. (a) Calculated Li ion diffusion coefficient of pristine (black) and LLT1 (red) from PITT tests. Impedance spectra (100 kHz to 100 mHz) of pristine (b) and LLT1 (c) obtained from the cell at 4.2 V. The insets are the equivalent circuit model used to fit the experimental model. Dashed lines are the CNLS fittings of the impedance spectra of the equivalent circuit model.

uniformly. The inset in Figure 3d clearly depicts the interface between the core material and the coating material.

3.2.2. Electrochemical Property Test. The electrochemical property testing of the pristine and coated electrodes were performed to examine the coating effect on cyclic performance, as well as the rate capability. Figure 5a displays the discharge capacity retention with a cutoff voltage of 4.4 V. As shown in the figure, materials with a LLTO coating (1, 2, and 5 wt %) maintained at least 99% capacity (compared to first discharge) after 10 cycles, while the pristine material only retained ~85% of the first cycle discharge capacity after 10 cycles. In this work, LLT1 was adopted as the representative sample for further in-depth investigation on the role of the LLTO coating material on the NCA electrodes.

Figures 5b and 5c show the rate testing data for pristine and LLT1 electrodes at the rate of C/20 for charging and C/20, C/10, C/5, C/2, 1C, and 2C for discharging, in the voltage range of 4.4−2.0 V. All the cells for rate testing are with a loading density of ~5 mg/cm^2. As can be seen from the graph, the capacity at C/20 has been improved from ~125 mAh/g to ~135 mAh/g; the improvement of the coated samples is most obvious at higher rates of C/2, 1C, and 2C. For C/2, 1C, and 2C, the capacities for the pristine electrode are 82, 68, and 44 mAh/g, respectively. On the other hand, the LLT1 electrode shows much higher capacity: 105, 93, and 82 mAh/g. In addition, the OCV drop for the pristine material at the beginning of each discharge is more severe at the higher rates. In the case of the 2C rate, the cell voltage of the pristine electrode drops to 3.45 V, while the LLT1 electrode remains at 4.0 V.

3.2.3. PITT Test Results. In order to further identify the reasons for the improved rate capability of the LLT1 electrode, a PITT test (details described in Figure S2 in the Supporting Information) was performed, and Li chemical diffusion coefficients in both pristine and LLT1-coated electrodes are extracted. The results obtained from a step size of 10 mV and current limit corresponding to a C/200 rate are shown in Figures S2a and 2b in the Supporting Information.The linearity of (ln I) vs t is good enough for the analysis shown below. A semilogarithmic plot of the current versus time was extracted based on the long-time dependence, $\tau \gg L^2/\tilde{D}_{Li}$. The lithium diffusion can be solved with Fick's law for a semi-infinite system with a perturbation of the surface concentration in eq 1:[27]

$$I(t) = \frac{2Fa(C_s - C_0)\tilde{D}}{L} \exp\left(-\frac{\pi^2\tilde{D}}{4L^2}t\right) \quad (1)$$

The lithium chemical diffusion coefficient was obtained from the slope of the linearity of ln (I) vs t in eq 2:

$$\tilde{D} = -\frac{\mathrm{d}\ln(I)}{\mathrm{d}t}\cdot\frac{4L^2}{\pi^2} \quad (2)$$

Figure 6a plots the calculated lithium diffusion coefficient ($\tilde{D}_{Li}$) versus the state of charge. The LLTO coating increases the chemical lithium diffusion coefficient by almost 1 order of magnitude at any state of charge (except for a voltage of 3.7−3.8 V), compared to that of the pristine electrode. Another interesting fact is that the valley of the diffusion coefficient profile moves from 3.65 V for the pristine electrode to 3.75 V for the LLT1 electrode. The valley in the diffusion coefficient plot is generally representative of a two-phase reaction, the value of which is usually two to three magnitudes of orders lower than the diffusion coefficient in the single-phase region.[28] There has also been a study on the two-phase reaction during

dx.doi.org/10.1021/cm300929r | Chem. Mater. XXXX, XXX, XXX−XXX

Table 1. Fitting Parameters of Pristine and LLT1 Positive Electrode, Determined from the CNLS Fitting of Impedance Spectra to the Equivalent Circuit Model Presented in Figures 4b and 4c

			CPE_f[a]			CPE_{dl}[a]			
	R_Ω (Ω)	R_f (Ω)	C (F $s^{\eta-1}$)	η	R_{ct} (Ω)	C (F·$s^{\eta-1}$)	η	A_ω (Ω $s^{-0.5}$)	Chi-Squared
pristine	1.64	2.17	1.19×10^{-4}	1	2.60	2.94×10^{-5}	0.83	34.77	0.0016
LLT1	1.81	0.79	4.65×10^{-6}	1	0.41	0.3×10^{-3}	1	16.77	0.0005

[a]Constant phase element (CPE) was expressed in the form of $C(j\omega)^\eta$.

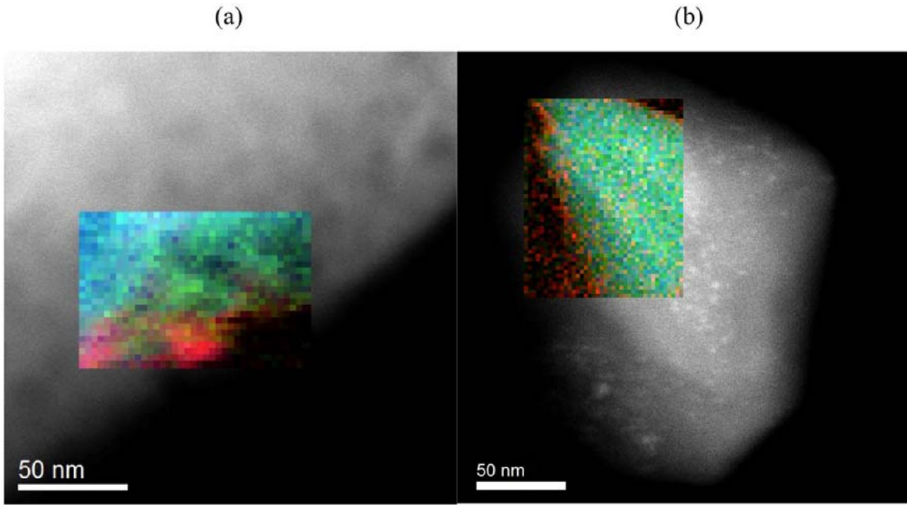

Figure 7. EELS mapping of LLT5 (a) before and (b) after cycling. (Legend: green denotes Li; blue denotes La; and red denotes Ti.)

the first charge of this material; and the valley is associated with the fact that another hexagonal phase would appear and coexist with the original hexagonal phase.[29] Generally, the LLTO coating layer delays the occurrence of a two-phase reaction by 0.1 V.

3.2.4. EIS Results. EIS measurements were carried out to study the effects of the LLTO coating on the interfacial characteristics between the electrolyte and the active materials. Figures 6b and 6c exhibit the impedance spectra of the active materials from the three-electrode cell configuration at a cell potential of 4.2 V. The impedance spectra consist of two semicircles in the high and intermediate frequency range and a line inclined in the low frequency. The two semicircles at the high and intermediate frequency are attributed to Li^+ ion transport through the SEI and interfacial charge-transfer reaction combined with electrochemical double-layer capacitive behavior, respectively. The latter inclined line is responsible for the solid-state lithium diffusion into the active material. For the quantitative analysis, the simplified equivalent circuits presented in the insets of Figures 6b and 6c were used. The values of all electrical parameters were taken from the CNLS (complex nonlinear least-squares) fitting method to the equivalent circuits, as summarized in Table 1.

As listed in Table 1, all reaction resistances in LLT1 electrode have relatively smaller numbers than those in the pristine electrode. The resistances of SEI films (R_f), interfacial charge transfer reactions (R_{ct}), and Warburg coefficient (A_w), which is due to the solid-state lithium diffusion in the active material, decreased by 64%, 84%, and 52%, respectively. This indicates that every elementary reaction step at the interface is considerably improved by the LLTO coating layer. In the very low-frequency (<10 mHz), however, the impedance behavior of LLT1 electrode is found to be different from that of the pristine electrode. (The data are not presented in this work.) The LLT1 impedance spectra have an additional semicircle at very low frequency. One possibility is that another charge transfer reaction happens at the interface between LLTO coating and the NCA active material, since there is a change in the local structures from LLTO to NCA.[30] Further investigation will be carried out to identify the charge-transfer mechanism.

3.2.5. STEM_EELS Mapping Results. STEM images as well as EELS mapping were performed to examine the existence of coating before and after cycling. The RGB composite mapping is depicted in Figure 7. Signals for Ti and La elements can be clearly seen from the EELS map (also shown in Figure S3 in the Supporting Information). It indicates that the coating will not get detached from the surface during cycling; therefore, it has a lasting effect after cycling.

4. DISCUSSIONS

In this study, first-principles calculations are performed to characterize LLTO, one of the solid electrolyte candidates, fast lithium-ion conductors. The fast lithium conductivity is supported by our first-principles calculation results. In the low-lithium-concentration scenario, even the highest activation barrier of Li in-plane diffusion is as low as 230 meV, which is much lower than the typical calculated Li diffusion barriers in layered compounds such as NCA.[31] For the high-lithium-concentration scenario, the highest barrier is ~390 meV. Such a discrepancy between the two models, however, is probably caused by the different numbers of vacancies in the same plane for the migrating Li ion. In our calculations, because of the size limitation of the model supercells, the barriers in the high-lithium-concentration model were calculated with only one vacancy adjacent to the migrating Li ion, while in low lithium concentration model, two vacancies were located besides the migrating Li ion. As suggested by previous study, the rate of nonperfect crystals is very sensitive to the density of discrete

dx.doi.org/10.1021/cm300929r | Chem. Mater. XXXX, XXX, XXX–XXX

vacancy sources.[32] Moreover, note that the relatively high diffusion barrier is reached only in a specific local environment, and barriers in other local environments can be as low as 22 meV. Since all computations are performed at 0 K, Li and La ions, as well as vacancies, are arranged in a highly ordered way. At room temperature, such site ordering is greatly reduced and the overall lithium diffusion activation energies should be lowered.[25]

This solid electrolyte candidate, LLTO, has been applied as a coating material to our NCA cathode material in lithium-ion half-cells. SEM, EDS, TEM, and XRD results consistently suggest that the coating material LLTO exists on the surface of the NCA material and it is crystalline in nature. Nevertheless, the shift of the XRD peaks for our samples of LLTO indicates larger interplane distances and, therefore, possible local structure change of the perovskite LLTO.

As shown in Figure 5a, the cycling performances of coated samples are significantly improved, which is consistent with a previous study on a different layered oxide.[33] Such improvement is generally attributed to the surface protection of the coating. For high-voltage cathode materials such as NCA, the high operating voltage may cause the decomposition of the $LiPF_6$ salt, generating HF in the electrolyte. For uncoated samples, the electrode surface is in directly contact with the electrolyte; thus, the active materials might be dissolved into the electrolyte, because of the HF etching.[34,35] Meanwhile, the electrode surface, which is unstable at high voltage, undergoes structural reconstruction and forms a spinel-like phase near the surface. This phenomenon is suggested by the large OCV drop at the beginning of each discharge for the uncoated sample in this study. The LLTO coating that exists on the electrode surface prevents the NCA materials from direct contact with the electrolyte and, therefore, can largely reduce the dissolution of active materials and suppress the surface structural change at high voltage. The capacity retention of the LLTO-coated samples is significantly improved as a result.

Besides the cycling performance, the rate capability of coated sample is also enhanced as indicated in Figures 5b and 5c. The high ionic conductivity of the LLTO coating materials is regarded as a key factor affecting the rate performance. Although the introduction of a coating layer creates another interface between the active material and the coating material, which may add an extra resistance to Li transportation, it is compensated by the fast lithium transportation inside the coating layer and the suppression of SEI formation. Therefore, the overall impedance is reduced significantly in the coated sample. As obtained from PITT results, the Li chemical diffusion coefficient in the LLTO-coated sample is 1 order of magnitude higher than that of the uncoated sample. The EIS results also show that the SEI layer impedance of the coated sample is much lower. For the LLT1 sample, the impedance for Li^+ diffusion in the SEI layer is even lowered by more than 60%. These observations suggest that the enhancement of the solid-state lithium diffusion caused by the LLTO coating should be an important contribution factor to the improved rate capability. This kinetic process may be an explanation for the delay of two-phase (the valley) in PITT results. Furthermore, the entire impedance for the active material is reduced for the LLTO-coated electrode, compared to the pristine electrode; this may be another reason for the higher voltage where two-phase reaction occurs.

Lastly, we note that the coating material would not decompose or detach from the NCA active material after cycling (cutoff voltage = 4.2 V) by STEM/EELS. It indicates that the coating has a lasting effect. A further study of LLTO coating will be carried out on other high-voltage cathode materials, such as high-voltage cathodes (cut-off voltage = 4.6−4.8 V), to determine whether the LLTO coating will continue to play a role in other higher voltage systems.

5. CONCLUSIONS

In summary, we demonstrated the significant improvement on rate capabilities and capacity retention on layered cathode material NCA by applying a fast ionic conduction solid electrolyte coating. We elucidate the mechanism of the solid electrolyte LLTO coating with a joint study of experiment and computation. LLTO has *intrinsically high* ionic conductivity. Therefore, besides acting as a protective coating layer, it reduces the impedance of Li^+ diffusion in the composite electrode, as well as the impedances of interfacial charge transfer and transportation through the SEI layer. In addition, the coating layer is relatively stable after cycling resulting in a continuous effect upon cycling. Our findings shed some new light on applying solid electrolyte as coating in high-voltage cathode materials and understanding the mechanism of coating in lithium-ion batteries. The stability of the LLTO coating material upon longer cycling, higher-voltage exposure (>4.5 V), and higher temperature exposure remains to be examined.

■ ASSOCIATED CONTENT

Ⓢ Supporting Information

This material is available free of charge via the Internet at http://pubs.acs.org.

■ AUTHOR INFORMATION

Corresponding Author

*E-mail: shirleymeng@ucsd.edu.

Notes

The authors declare no competing financial interest.

■ ACKNOWLEDGMENTS

The authors would like to acknowledge the financial support by Chemat Technology, Inc., under the Air Force SBIR (Contract No. FA9453-10-M-0115) and UCSD new faculty startup funding. STEM-EELS is carried out at the ORNL Shared Research Equipment (SHaRE) User Facility, which is sponsored by the Office of Basic Energy Sciences, U.S. Department of Energy. D.Q. acknowledges the use of the UCSD Cryo-Electron Microscopy Facility in Dr. Timothy S. Baker's group and the assistance from Dr. Albina Borisevich, Dr. Miaofang Chi from ORNL, and Mr. Qiang Wei. D.Q. and B.X. acknowledge Dr. S. Curtarolo and co-workers for providing the *aconvasp* code, together with the Texas Advanced Computing Center (TACC) at the University of Texas at Austin, for providing computational resources under project TG-DMR-110008.

■ REFERENCES

(1) Inaguma, Y.; Itoh, M. *Solid State Ionics* **1996**, *86−8*, 257.
(2) Inaguma, Y.; Katsumata, T.; Itoh, M. *Electrochemistry* **2000**, *68*, 534.
(3) Inaguma, Y.; Katsumata, T.; Itoh, M.; Morii, Y. *J. Solid State Chem.* **2002**, *166*, 67.
(4) Inaguma, Y.; Katsumata, T.; Itoh, M.; Morii, Y.; Tsurui, T. *Solid State Ionics* **2006**, *177*, 3037.

(5) Inaguma, Y.; Matsui, Y.; Shan, Y. J.; Itoh, M.; Nakamura, T. *Solid State Ionics* **1995**, *79*, 91.
(6) Stramare, S.; Thangadurai, V.; Weppner, W. *Chem. Mater.* **2003**, *15*, 3974.
(7) Harada, Y.; Hirakoso, Y.; Kawai, H.; Kuwano, J. *Solid State Ionics* **1999**, *121*, 245.
(8) Inaguma, Y.; Chen, L. Q.; Itoh, M.; Nakamura, T.; Uchida, T.; Ikuta, H.; Wakihara, M. *Solid State Commun.* **1993**, *86*, 689.
(9) Lee, J. m.; Kim, S. h.; Tak, Y.; Yoon, Y. S. *J. Power Sources* **2006**, *163*, 173.
(10) Abe, T.; Sagane, F.; Ohtsuka, M.; Iriyama, Y.; Ogumi, Z. *J. Electrochem. Soc.* **2005**, *152*, A2151.
(11) Hara, M.; Nakano, H.; Dokko, K.; Okuda, S.; Kaeriyama, A.; Kanamura, K. *J. Power Sources* **2009**, *189*, 485.
(12) Xu, B.; Fell, C. R.; Chi, M. F.; Meng, Y. S. *Energy Environ. Sci.* **2011**, *4*, 2223.
(13) Cho, H. M.; Park, Y. J.; Shin, H. C. *J. Electrochem. Soc.* **2010**, *157*, A8.
(14) Cho, H. M.; Park, Y. J.; Yeon, J. W.; Shin, H. C. *Electron. Mater. Lett.* **2009**, *5*, 169.
(15) Catti, M. *Chem. Mater.* **2007**, *19*, 3963.
(16) Catti, M. *J. Phys. Chem. C* **2008**, *112*, 11068.
(17) Kresse, G.; Joubert, D. *Phys. Rev. B: Condens. Matter Mater. Phys.* **1999**, *59*, 1758.
(18) Kresse, G.; Furthmuller, J. *Phys. Rev. B* **1996**, *54*, 11169.
(19) Kresse, G.; Hafner, J. *Phys. Rev. B: Condens. Matter Mater. Phys.* **1994**, *49*, 14251.
(20) Dudarev, S. L.; Botton, G. A.; Savrasov, S. Y.; Humphreys, C. J.; Sutton, A. P. *Phys. Rev. B: Condens. Matter Mater. Phys.* **1998**, *57*, 1505.
(21) Liechtenstein, A. I.; Anisimov, V. I.; Zaanen, J. *Phys. Rev. B: Condens. Matter Mater. Phys.* **1995**, *52*, R5467.
(22) Setyawan, W.; Gaume, R. M.; Feigelson, R. S.; Curtarolo, S. *IEEE Trans. Nucl. Sci.* **2009**, *56*, 2989.
(23) Lang, J. K.; Baer, Y.; Cox, P. A. *J. Phys. F: Metal Phys* **1981**, *11*, 121.
(24) Henkelman, G.; Jonsson, H. *J. Chem. Phys.* **2000**, *113*, 9978.
(25) Okumura, T.; Ina, T.; Orikasa, Y.; Arai, H.; Uchimoto, Y.; Ogumi, Z. *J. Mater. Chem.* **2011**, *21*, 10195−10205.
(26) Fourquet, J. L.; Duroy, H.; Crosnier-Lopez, M. P. *J. Solid State Chem.* **1996**, *127*, 283.
(27) Xia, H.; Lu, L.; Ceder, G. *J. Power Sources* **2006**, *159*, 1422.
(28) Xie, J.; Imanishi, N.; et al. *Electrochim. Acta* **2009**, *54*, 4631−4637.
(29) Yoon, W.-S.; Chung, K. Y.; et al. *Electrochem. Commun.* **2006**, *8*, 1257−1262.
(30) Barsoukov, E.; Macdonald, J. R. *Impedance Spectroscopy: Theory, Experiment, And Applications*; 2nd ed.; Wiley−Interscience: Hoboken, NJ, 2005.
(31) Kang, K. S.; Meng, Y. S.; Breger, J.; Grey, C. P.; Ceder, G. *Science* **2006**, *311*, 977.
(32) Van der Ven, A.; Yu, H.-C.; et al. *Prog. Mater. Sci.* **2010**, *55*, 61−105.
(33) Lee, H. J.; Park, Y. J. *Bull. Korean Chem. Soc.* **2010**, *31*, 3233−3237.
(34) Myung, S. T.; Cho, M. H.; Hong, H. T.; Kang, T. H.; Kim, C. S. *J. Power Sources* **2005**, *146*, 222.
(35) Myung, S. T.; Izumi, K.; Komaba, S.; Yashiro, H.; Bang, H. J.; Sun, Y. K.; Kumagai, N. *J. Phys. Chem. C* **2007**, *111*, 4061.